



Photochromism in oxalatonibates†

Cite this: DOI: 10.1039/c7dt04077f

 Alexandra A. Shmakova,^{a,b} Eugeniy M. Glebov,^{b,c} Valeri V. Korolev,^b
 Dmitri V. Stass,^{b,c} Enrico Benassi,^{*b,d} Pavel A. Abramov^b  ^{*a,b} and
 Maxim N. Sokolov^b  ^{a,b}

Received 29th October 2017.

Accepted 2nd January 2018

DOI: 10.1039/c7dt04077f

rsc.li/dalton

Addition of 2,2'-bipyridine (bpy), 1,10-phenanthroline (phen) or 2-aminopyridine (2-NH₂-py) to aqueous solutions of (NH₄)[NbO(C₂O₄)₂(H₂O)₂]·3H₂O (Nb-Ox) yields tris-oxalate complexes (bpyH₂)(bpyH)[NbO(C₂O₄)₃]·2H₂O (**1**), (phenH)₃[NbO(C₂O₄)₃]·3H₂O (**2**), and (2-NH₂-pyH)₃[NbO(C₂O₄)₃]·2H₂O (**3**), which were characterised by XRD, IR and EA. Bipyridinium salt **1** demonstrates remarkable photoactivity even under irradiation by daylight. The nature of the photoactivity was studied by diffuse reflectance (DR) spectroscopy, ESR and quantum-chemical calculations.

Introduction

Oxalate C₂O₄²⁻ is ubiquitous in coordination chemistry. The M/C₂O₄²⁻ stoichiometry in oxalate complexes ranges from 1 : 1 up to 1 : 5. Moreover, oxalate often acts as a bridging ligand in homo- and heterometallic compounds with open-framework architectures¹ and important magnetic and optical properties.²

Ferrioxalate, a common chemical actinometer, has rich photochemistry.³⁻⁷ A noteworthy application of OH radicals, photoproduced from ferrioxalate, involves oxidative decontamination of organic substances in natural and industrial systems.^{3,8} V^{II} and V^{III} are involved in heterometallic oxalates with magnetic ordering.⁹

Early transition metals with higher coordination numbers mainly form tetrakis(oxalato)metalates [M(C₂O₄)₄]ⁿ⁻ (M = Zr^{IV},^{10,11} Hf^{IV},^{3,12} Nb^{IV},^{13,14} U^{IV},^{15,16} and Yb^{III}¹⁷). For Nb, both Nb^{IV} and Nb^V form oxalate complexes. Three structures have been reported for Nb^{IV} oxalate complexes K₄[Nb(C₂O₄)₄]·3H₂O, K₂(H₃NCH₂CH₂)₂[Nb(C₂O₄)₄]·4H₂O¹³ and K₄[Nb(C₂O₄)₄]·4H₂O·1/2H₂C₂O₄.¹⁴ Nb^V typically forms tris(oxalato)oxoniobates(v), [NbO(C₂O₄)₃]³⁻,¹⁸⁻²⁰ even though one oxalate can be replaced with two aqua ligands, as in the commercially available (NH₄)[NbO(C₂O₄)₂(H₂O)₂]·3H₂O (Nb-Ox).²¹ Recently some

mixed oxalates have been reported.²²⁻²⁴ Niobium oxide-based materials are efficient photocatalytic materials.²⁵⁻²⁸ However, photochemical potential of niobium oxalates remains unexplored. Taking into account well documented photoactivity of niobium oxide-based materials, on the one hand, and that of coordinated oxalates, on the other hand, Nb oxalates are worthy of investigation. In this study, we obtained three novel salts of [NbO(C₂O₄)₃]³⁻ with different protonated N-heterocyclic cations and explored their photochemical behaviour.

Results and discussion

Preparation and structure of 1-3

In aqueous solution, (NH₄)[NbO(C₂O₄)₂(H₂O)₂]·3H₂O (Nb-Ox) equilibrates with several species, including the tris-oxalate complex [NbO(C₂O₄)₃]³⁻.²⁹ We prepared salts of [NbO(C₂O₄)₃]³⁻ with protonated N-heterocyclic cations by the addition of stoichiometric amounts of solid bpy, phen, or 2-NH₂-py to aqueous solution of Nb-Ox. Apparently, the initial [NbO(C₂O₄)₂(H₂O)₂]⁻ anion rearranges into [NbO(C₂O₄)₃]³⁻, and this equilibrium is shifted due to poor solubility of the salts with N-protonated heterocyclic cations. Crystal structures of (bpyH₂)(bpyH)[NbO(C₂O₄)₃]·2H₂O (**1**), (phenH)₃[NbO(C₂O₄)₃]·3H₂O (**2**), and (2-NH₂-pyH)₃[NbO(C₂O₄)₃]·2H₂O (**3**) were determined by single crystal X-ray diffraction (XRD). In all cases, the Nb atom in [NbO(C₂O₄)₃]³⁻ has a pentagonal-bipyramidal coordination by three asymmetrically coordinated oxalate ligands (d(Nb–O) = 2.110(2)–2.206(2) Å), and a terminal oxo ligand (d(Nb=O) = 1.719(2)–1.730(2) Å) (the Nb–O distances are listed in Table S2†). The [NbO(C₂O₄)₃]³⁻ anion (Fig. 1) forms strong hydrogen bonds with water molecules and cations, which explains low solubility and easy crystallization of **1–3**. Relevant

^aNikolaev Institute of Inorganic Chemistry SB RAS, 3 Akad. Lavrentiev Ave, 630090 Novosibirsk, Russia. E-mail: abramov@niic.nsc.ru

^bNovosibirsk State University, 2 Pirogova Str., 630090 Novosibirsk, Russia. E-mail: glebov@kinetics.nsc.ru, enrico.benassi@sns.it

^cVoevodsky Institute of Chemical Kinetics and Combustion, Institutskaya str. 3, 630090 Novosibirsk, Russia

^dSchool of Science and Technology, Nazarbayev University, 53 Kabanbay Batyr Ave, Astana 010000, Republic of Kazakhstan

† Electronic supplementary information (ESI) available. CCDC 1581634–1581636. For ESI and crystallographic data in CIF or other electronic format see DOI: 10.1039/c7dt04077f

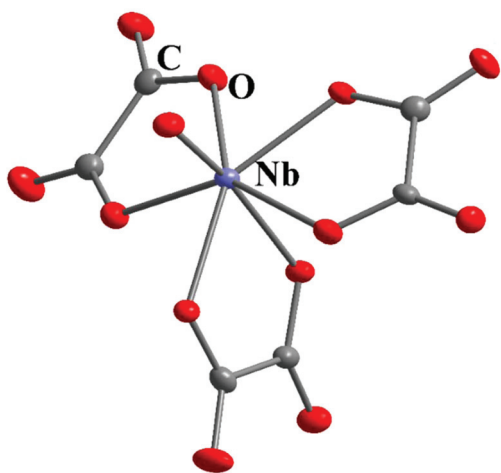


Fig. 1 View of $[\text{NbO}(\text{C}_2\text{O}_4)_3]^{3-}$. Displacement ellipsoids shown with 50% probability.

information about the geometry of hydrogen bonds is summarized in Tables S3–S5.† Attempts to use viologens that lack hydrogen bond donors as cations failed to yield crystalline products.

In the structure of **1** the three acidic protons were located directly from XRD experiments near nitrogen atoms of bpy to compensate the anionic charge. These protons participate in the hydrogen bonding between bpyH^+ cations and oxalate ligands. Such protons can shuttle between the cations and oxalate anions in the solid state. The crystal packing of **1** is chiral due to the formation of chiral chains running along the [100] direction, comprising both bpyH^+ cations and anions, connected through hydrogen bonds (Fig. S1†).

In the structure of **2** all phen are monoprotonated. Only one phenH^+ cation participates in a weak ($d(\text{O4}\cdots\text{N6}) = 2.81(1) \text{ \AA}$) hydrogen bond with an oxalate ligand of the $[\text{NbO}(\text{C}_2\text{O}_4)_3]^{3-}$ anion (Fig. S2†). Other cations are connected only with water molecules. The phenH^+ cations are also involved in π - π stacking interactions (*ca.* 3.4 Å), forming infinite columns (Fig. S3 and S4†).

In the structure of **3** exclusive protonation of the pyridine nitrogen is detected, while the NH_2 groups participate only in hydrogen bonding. This is in agreement with the relative basicity of the respective nitrogen atoms. Oxalate ligands form different H-bonds with cations and water molecules of crystallization (Fig. S5†). One sort of oxalate is connected only with pyridinium-attached protons from two cations. Another sort forms hydrogen bonds with two water molecules and two amino groups. The remaining oxalate is connected with three NH_2 groups and one water molecule. The aminopyridinium cations pack as three-molecule associates connected by π - π stacking interactions (*ca.* 3.5 Å). These aggregates arrange along the [001] crystal direction (Fig. S6†).

UV spectroscopy and photodegradation of **1** in aqueous solutions

Concentration-dependent spectra of **1** in aqueous solutions are shown in Fig. S7.† Beer's law is fulfilled at $\leq 3 \times 10^{-5} \text{ M}$;

increase in concentration results in evident changes in spectral shape and deviations from Beer's law. At low concentrations the spectrum exhibits a wide band with the maximum at 239 nm ($\epsilon = 39\,900 \text{ M}^{-1} \text{ cm}^{-1}$), and a shoulder at 268 nm ($\epsilon = 18\,500 \text{ M}^{-1} \text{ cm}^{-1}$). The real spectrum is thus the superposition of the spectra of the two individual species – bpyH^+ (which is in equilibrium with bpy, $\text{p}K_{\text{a}} = 5.25$ (ref. 30)) and $[\text{NbO}(\text{Ox})_3]^{3-}$. The deviation from Beer's law is probably explained by equilibrium between bpy, bpyH^+ and bpyH_2^{2+} , formation of bpyH^+ dimers or larger associates, proton transfer from bpyH^+ to oxalate, or, eventually, $\{(\text{bpyH})[\text{NbO}(\text{Ox})_3]^{2-}\}$ ionic pairs.

The UV spectrum of $[\text{NbO}(\text{Ox})_3]^{3-}$ in aqueous solutions was extracted from the observed spectrum of **1** below $3 \times 10^{-5} \text{ M}$, when Beer's law is obeyed (curve 1 in Fig. S8†), and the bpy spectrum was taken from ref. 31 (curve 2 in Fig. S8†). The difference between the spectrum of **1** and the doubled spectrum of bpy yields the spectrum of the $[\text{NbO}(\text{Ox})_3]^{3-}$ species (curve 3 in Fig. S8†). This spectrum contains an intense band at 221 nm and a shoulder at *ca.* 234 nm, both corresponding to LMCT from Ox^{2-} to $\text{d}^0\text{-Nb}^{5+}$. Note that the gas phase DFT calculations of the electronic absorption spectrum of **1** (see below) produce a single narrow band at $\lambda_{\text{abs}} = 256 \text{ nm}$. The calculated absorption transition involves excitation, mainly localised on the bpyH^+ cations, with a minor contribution of excitation localised on the nearest oxalates. Therefore, we have a satisfactory agreement between the experimental spectrum in aqueous solutions and the calculated spectrum in the gas phase. The tail of the LMCT band extending to the near UV spectral region is responsible for the photochemical activity of **1** in the solid state.

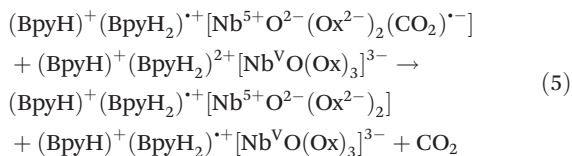
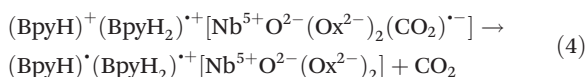
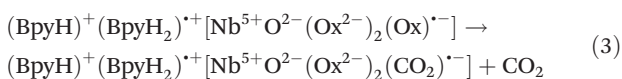
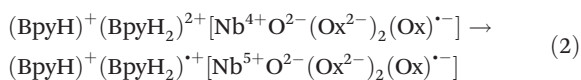
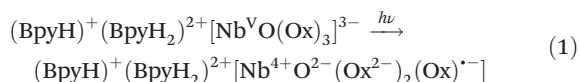
Irradiation of aqueous solutions of **1** in the near-UV region results in slow photodegradation (Fig. S9†). The absence of isosbestic points testifies independent photochemical processes for the bpyH^+ cation and $[\text{NbO}(\text{Ox})_3]^{3-}$ complex, with comparable quantum yields. Photochemistry of aqueous bpy (equilibrium with bpyH^+) is rather complicated; several species (^3bpy (triplet state) and several types of free radicals) were detected in time-resolved experiments.^{32–34} For the $[\text{NbO}(\text{Ox})_3]^{3-}$ complex, one might expect photoredox processes starting from inner-sphere electron transfer from Ox^{2-} to Nb^{5+} , typical of oxalate complexes of other transition metals (*e.g.*, photochemistry of ferrioxalate).^{35–37} Due to the vastness and complexity of the topic, liquid-state photochemistry of **1** will be described in a separate contribution elsewhere. For our current purpose it is sufficient to emphasize that no reversible photochemical reactions were observed.

Photoactivity of solids **1–3**

Polycrystalline powder of **1** is light-sensitive. Near-UV irradiation results in dark-blue coloration. The diffuse reflection (DR) spectrum (Kubelka–Munk function) is shown in Fig. S10† (curve 1). When irradiation time was short (several seconds, Fig. S10†), the coloration disappeared almost completely in a couple of hours (Fig. S10†). After this thermal discoloration it was possible to restore coloration by repeating irradiation. No visible photodegradation (monitored by

residual DR) occurred. Therefore, in the solid state **1** behaves as a T-type photochromic system (with thermal backward reaction).³⁸ No photochromism was observed in aqueous solution.

The light-induced coloration of **1** is accompanied by an ESR signal (curve 1 in Fig. S11†). The ESR spectrum is a single line with a half-width of 10 G (narrow light-induced signal from quartz also appears as a result of quartz ampoule irradiation). The ESR signal disappears both in the dark (curve 2 in Fig. S11†), and after irradiation by visible light (“light annealing”, curve 3 in Fig. S11†). The appearance and decay of the ESR signal correlate with that of blue coloration. The kinetic behaviour of both blue coloration and ESR signals in the dark is complicated and depends on the irradiation time (to be discussed below). The ESR signal can be restored by UV irradiation.



Therefore, **1** demonstrates both T-type and P-type photochromic behaviour, when both thermal and photochemical discolorations are possible.

In addition to DR and ESR techniques, IR spectra of UV-irradiated samples were recorded (Fig. S12†). The only IR-detected radiation-induced effect was an increase in the intensity of the band attributable to free CO₂ bands. No signature of bulk structural changes was observed, which is probably explained by low sensitivity of the IR technique to surface reactions.

For **2**, light-induced coloration was also observed (Fig. S13†), and a very weak singlet ESR signal with a half-width of 13 G appeared after prolonged (tens of minutes) irradiation (Fig. S14†). In the case of **3** neither light-induced coloration (Fig. S15†) nor ESR signals were detected. Hence, the photochemical properties of **1**–**3** are strongly dependent on the counter-cations. We believe that the species responsible for the coloration and ESR signal in **1** is the radical cation of bpyH₂²⁺, namely bpyH₂^{•+} (Scheme S1†). The viologens, the simplest of which is bpyH₂²⁺ dication itself, are well-known to form very stable blue radical cations.³⁹ The most common is methyl viologen (MV²⁺), regarded as an organic photochromic

system due to reversible redox reactions.⁴⁰ Solid-phase reduction of MV²⁺ to MV^{•+} upon thermolysis and photolysis is well known.⁴¹ The ESR spectra of viologenic radical cations in solutions demonstrate typical hyperfine splitting (HFS).^{40,41} In the polycrystalline state HFS is averaged due to random orientation, and ESR spectra appear as single lines with a linewidth of ca. 10 G.⁴² Note that the ESR spectrum in **1** cannot be attributed to the oxalate radical anion, which shows a very sharp ESR signal (narrower than 1 G⁴³). Also, the anisotropic powder spectrum of the CO₂^{•-} radical⁴⁴ was not detected.

The mechanism of bpyH₂^{•+} formation in the course of photolysis of **1** is not evident. The possibility of direct photo-induced electron transfer from the coordinated Ox²⁻ anion to the bipyridinium counter-ion was examined by checking photolysis of solid bipyridinium oxalate (**4**). No coloration was produced. The absence of photochemistry in this case can be explained by the absence of the absorption bands corresponding to the charge transfer from bpyH₂²⁺ to [NbO(Ox)₃]³⁻. The LMCT band is thus necessary to start the photochemical reaction. Therefore, the primary process of light absorption, excitation transfer to the anion, the Nb=O π-bond cleavage and the light-induced electron transfer (eqn (1)) from oxalate to Nb⁵⁺ is followed by secondary electron transfer from Nb⁴⁺ to bpyH₂²⁺ (eqn (2)).

The (bpyH)^{•+}(bpyH₂)²⁺[Nb⁵⁺O²⁻(Ox²⁻)₂(Ox)^{•-}] “biradical” couple, thus produced, if sufficiently stable, could be the species responsible for coloration. Nevertheless, it cannot be the same species as detected in the ESR spectrum, because the latter features neither the characteristic narrow signal of C₂O₄^{•-},⁴³ nor the anisotropic CO₂^{•-} spectrum.⁴⁴ One can propose that after rapid decarboxylation of the oxalate radical (eqn (3)), the resulting CO₂^{•-} reduces either bpyH^{•+} (eqn (4); further reduction of bpyH₂^{•+} is also possible) or bipyridyl dication (eqn (5)), providing the “relay transfer” of free valence. In this case, the migration of free valence can be accompanied by the migration of bpyH^{•+} with the formation of (bpyH₂)^{•+}[Nb⁵⁺O²⁻(Ox²⁻)₂]⁻ and (bpyH₂)²⁺(bpyH₂)^{•+}[Nb⁵⁺O²⁻(Ox²⁻)₃]³⁻. Another possibility is just to transfer a proton, leaving bpy in close proximity to (bpyH₂)^{•+}[Nb⁵⁺O²⁻(Ox²⁻)₂]⁻ and producing (bpyH₂)²⁺(bpyH₂)^{•+}[Nb⁵⁺O²⁻(Ox²⁻)₃]³⁻. In the case of methyl viologen, the reduction of MV²⁺ by CO₂^{•-} in aqueous solutions is a diffusion-controlled reaction.⁴⁵

Probably, both (bpyH₂)^{•+}[Nb⁵⁺O²⁻(Ox²⁻)₂]⁻ and (bpyH₂)²⁺(bpyH₂)^{•+}[Nb⁵⁺O²⁻(Ox²⁻)₃]³⁻ species can be responsible for coloration and ESR spectra. An alternative reaction pathway could be represented by the oxidation of CO₂^{•-} radical anions by O₂ with the formation of superoxide radical O₂^{•-} (in aqueous solutions this reaction is fast enough; its rate constant is only an order of magnitude below the rate constants of diffusion-controlled reactions⁴⁶). The reversibility of photo-reduction on **1** can thus be explained by re-oxidation of bpyH₂^{•+} with dioxygen. The restoration of the original charges makes the system ready for the next cycle of coloration–decoloration, in spite of possible changes in the structure of the complex caused by irreversible destruction of oxalate. Limited per-

meability of crystals to atmospheric oxygen seems to be the reason for the complicated kinetics of the backward reaction.

Kinetics of the backward reaction

A thermal backward reaction was monitored by DR and ESR (Fig. S16a and S16b† correspondingly). For DR spectra the Kubelka–Munk function (proportional to the concentration of the light-absorbing centres) was used to measure the concentration. For ESR spectra we used the amplitudes of the signals instead of the second integrals, because the shape of the signal did not change along the course of the reaction.

The main result of these kinetic measurements is that the characteristic lifetime of active centres depends on the irradiation lifetime. The longer irradiation time results in deeper migration of the active centres inside the crystals and, logically, in longer characteristic lifetimes.

Fig. S16a† shows a kinetic curve after short irradiation as monitored by diffuse reflection. The kinetics is described by using the Kohlrausch–Williams–Watts (KWW) empirical equation⁴⁷

$$c(t) = c_0 \exp[-(t/\tau)^\beta] \quad (6)$$

where τ is the averaged characteristic time of the process, and the parameter β ranges from 0 to 1.⁴⁸ The KWW equation is often employed for the description of kinetics in the solid state, where the distribution of rate constants for individual molecules exists, and typically, the values of parameter β are around 0.5.⁴⁹ The best fit for the kinetic curve (Fig. S16a†) gives $\beta = (0.42 \pm 0.03)$ and $\tau = (530 \pm 70)$ s. The explanation of the KWW behaviour within the framework of the proposed reaction scheme is the stabilization of the radical cations at different distances from the polycrystalline surface (*e.g.*, due the “relay” process). The deeper the radical cation from the surface, the more long-living it is and the lower the probability of its reoxidation. The irradiation time necessary to accumulate a strong enough ESR signal is usually longer than for the DR signal, which results in longer decay times, as determined from ESR. An example is shown in Fig. S16b,† where the kinetic curve is fitted by the monoexponential function with the characteristic lifetime (1470 ± 150) s. For one of the samples the half-life, measured from ESR, was 10 days.

Quantum mechanical calculations

These experimental findings were supported by DFT calculations. Theoretical investigation was restricted to **1**. According to X-ray data, **1** is written as $(\text{bpyH}_2)(\text{bpyH})[\text{NbO}(\text{C}_2\text{O}_4)_3] \cdot 2\text{H}_2\text{O}$. Upon geometry optimisation, the stable form of **1** shows both bpy as being singly protonated, while the third proton goes to one of the oxalate ligands, *viz.* $(\text{bpyH})_2[\text{NbO}(\text{C}_2\text{O}_4)_2(\text{C}_2\text{O}_4\text{H})] \cdot 2\text{H}_2\text{O}$. The topological analysis confirms that the proton is mainly bonded with oxalate, but the proton exchange requires only 2.1 kJ mol⁻¹. This proton is, strictly speaking, located between a nitrogen atom of one bpyH^+ and an oxygen atom of the oxalate ligand closest to it. In the following discussion, to

be consistent, we shall consider only $(\text{bpyH})_2[\text{NbO}(\text{C}_2\text{O}_4)_2(\text{C}_2\text{O}_4\text{H})] \cdot 2\text{H}_2\text{O}$.

Regarding the appearance of the blue coloration after irradiation of **1**, QM calculations assume initial photoisomerisation: upon absorption of light quanta (at 250 nm) the system undergoes a remarkable change in geometry (mainly around the $\{\text{NbO}\}^{3+}$ ion and in the positions of the acidic protons, see below). The ground state (GS) potential energy hypersurface shows two minima: one is “colourless” and the other is “colourful” (blue; see Fig. S17a†). GS in the colourless minimum is photoexcited (250 nm) in agreement with the absorption peak: the system undergoes an electronic transition to the Frank–Condon region in the first bright singlet excited state (ES); this absorption does not induce geometry change, which still corresponds to the “colourless” GS minimum. There is a certain distribution among the vibrational levels that broadens the band shape, as follows from the vibronic calculation. After initial absorption the system undergoes molecular relaxation in ES, until it reaches a point from which it goes down to the GS through a non-radiative way (very likely *via* triplets). The region of the GS potential energy hypersurface to where the system “jumps down” is now far removed from the previous minimum, due to significant changes in geometry. Subsequently, the system relaxes on the GS and reaches another minimum, the “colourful” one, close to the point to where it had “jumped down” from the ES in the space of the internal coordinates. This minimum corresponds to a different geometry and electronic structure (*vide postea*). It corresponds to blue coloration since the energy gap between it and ES is narrower than for the “colourless” minimum (absorbing in the UV); when this minimum is populated, the absorption shifts to the red region.

In reference to Fig. S17b,† the absorption spectrum of the compound in its “colourless” minimum is characterised by a narrow transition band, centred at $\lambda = 256.4$ nm. This excitation is dominated by 0–0' transition. The absorption transition involves excitation basically localised on the bpyH^+ cations (with minor contribution from the nearest oxalates), from H to L and from H–1 to L+1 (Fig. 2, left). The absorption spectrum of the compound in its “colourful” minimum is characterised by a broad band, showing a partial vibronic resolution underneath. The maximum is located at $\lambda = 576.8$ nm. The transition is mainly L+1 to H. In this case we observe a strong charge transfer character (Fig. 2): upon absorption of a photon, the charge density moves from the central moiety of the complex (NbO^{3+} plus oxalate ions) to a bpyH^+ cation.

As for molecular geometries, in both the GS minima and the ES optimised geometry, the Nb atom retains its pentagonal bipyramidal coordination. An apex is occupied by O^{2-} , whereas the remaining six positions are occupied by as many oxygen atoms from three bidentate oxalates. In the “colourful” GS minimum we observe a remarkable change in the geometry. In particular, both bpyH^+ change their orientation with respect to the anion (Fig. S18a and b†). One bpyH^+ cation undergoes intramolecular proton transfer, from bpy

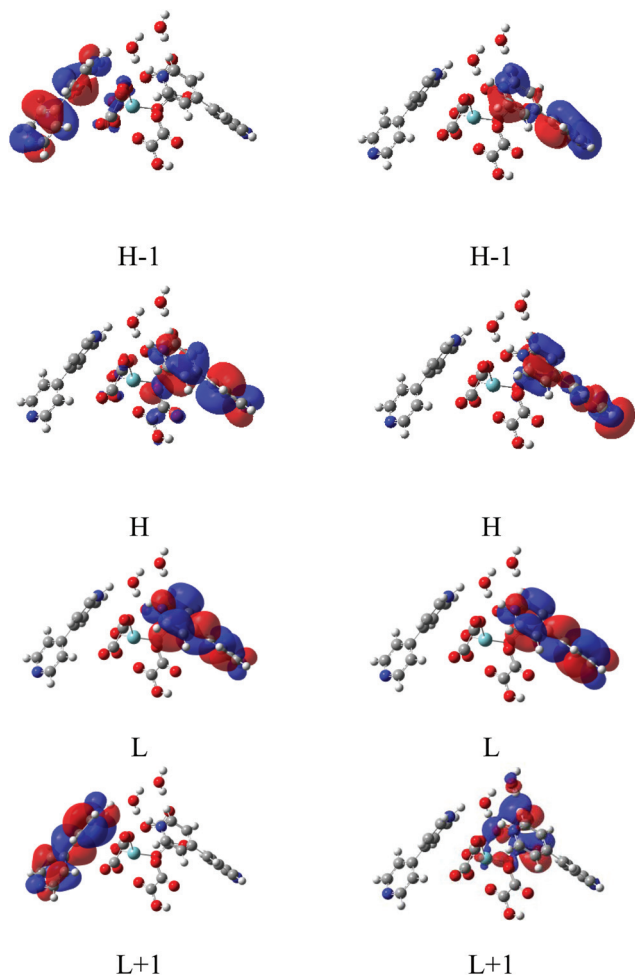


Fig. 2 Plot of the frontier MOs for the “colourless” (left) and “colourful” minima (right). All isosurfaces are visualised with $|\text{isovalue}| = 0.004$ a.u. Legend of colours for atomic species: white (H), grey (C), blue (N), red (O), and light blue (Nb).

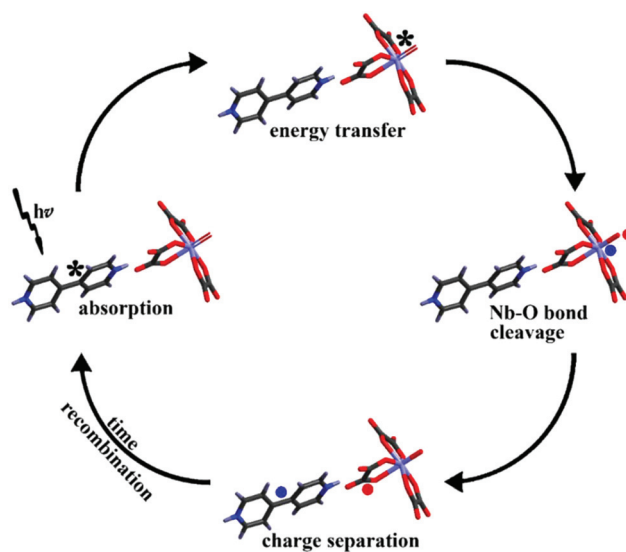
(“internal”, closer to the {NbO}-kernel) to the coordinated oxalate (“external”, farther from the {NbO}-kernel). Photo-induced proton transfer and acidochromism are quite common in pyridinium derivatives.⁵⁰ The oxalate complex itself does not show remarkable changes in geometry: we observe only that (a) the Nb=O bond stretches by 0.02 Å, (b) the Nb–O_{oxalate} bonds become shrunk by 0.01 Å, (c) the “equatorial” pentagon of the bipyramide becomes more regular, and (d) in the “colourless” minimum the Nb is slightly out-of-plane of the pentagon, whereas in the “colourful” minimum it sits perfectly at the centre of it. The intramolecular interactions were also investigated by means of the reduced density gradient analysis (Fig. S18c and d[†]). The attractive interactions (depicted in blue when strong, in turquoise when weak) are observed between Nb and apical O_{oxalate}, between water and the nearest oxalate ion, between oxygen atoms of different oxalate ions, and between oxalate ions and bpyH⁺. These regions of attractive interactions are often close to the regions of repulsive interactions, such that the stabilization is partially

reduced. This implies a certain “floppiness” of the complex that may ease structural changes.

To verify the hypothesis of energy transfer between bpyH⁺ and the central {NbO}-containing moiety (see Scheme 1), we computed the exciton transfer (or electronic energy transfer, EET) coupling. To this aim, the system was partitioned into three moieties: two donors (represented by the bpyH⁺ ligands; Fig. 3, highlighted in red and green, namely D₁ and D₂) and one acceptor (represented by the central core; Fig. 3, highlighted in blue, namely A). The EET coupling matrix element T_{EET} was computed between the pairs D₁-A and D₂-A. For both pairs, strong coupling was found; in particular, the EET coupling is stronger for D₂-A than for D₁-A, *viz.* $T_{\text{EET}}(\text{D}_1\text{-A}) = -8.1$ meV and $T_{\text{EET}}(\text{D}_2\text{-A}) = -25.0$ meV. This is straightforwardly explained on the basis of the orientation and distance of the energy donors with respect to the acceptor. In both cases, the main contributions to the coupling are the dipole-dipole and the dipole-octupole interactions.

We finally investigated the charge separation after the EET (Fig. 3). The geometries of $[\text{NbO}(\text{C}_2\text{O}_4)_3]^{2-}$ and (bpyH)[•] were fully optimised in the gas phase, and their spin density were computed and plotted (Fig. S19[†]). In the case of $[\text{NbO}(\text{C}_2\text{O}_4)_3]^{2-}$, the spin density is mostly localised on the oxalate ion that equatorially and apically coordinates Nb, on the O atom of {NbO}, and on Nb (Fig. S19a[†]).

In (bpyH)[•] the spin density is localised on one of the two py rings, more specifically, on the non-protonated one (Fig. S19b[†]), that is, on the py closer to the central moiety of **1**. The *g*-tensor computed for the (bpyH)[•] radical confirms the experimental attribution of the ESP spectrum (Table S6[†]). Scheme 1 depicts the energy transfer/electron transfer cycle, as follows from DFT calculations. However, as discussed above, this scheme is complicated by irreversible degradation of oxalate and “relay” on the paramagnetic centres and protons.



Scheme 1 Proposed mechanism of complex **1** photoactivity (without subsequent chemical reactions).

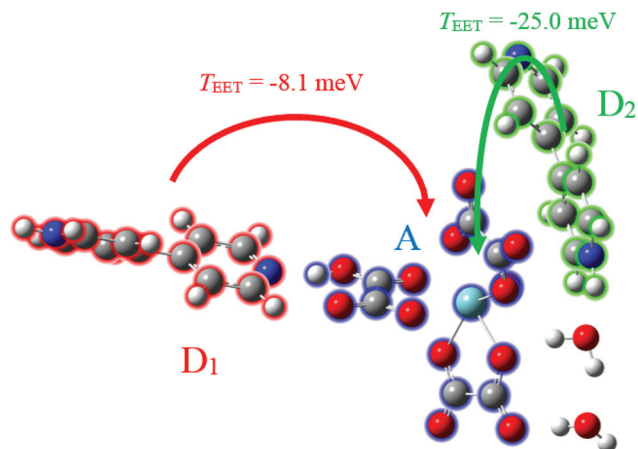


Fig. 3 Scheme representing the two donors, D₁ and D₂ (viz., bpyH⁺) and the acceptor, A, involved in the energy transfer. The values of the EET coupling matrix elements are also depicted.

Conclusions

A set of heterocyclic nitrogen bases was used to prepare new niobium tris-oxalate complexes: (bpyH₂)(bpyH)[NbO(C₂O₄)₃]·2H₂O (1), (phenH)₃[NbO(C₂O₄)₃]·3H₂O (2), and (2-NH₂-pyH)₃[NbO(C₂O₄)₃]·2H₂O (3) salts by an equilibrium shift in aqueous solutions of [NbO(C₂O₄)₂(H₂O)₂]⁻. Complex 1 demonstrates intense blue photocolouration under daylight irradiation. We proposed the mechanism of the process as the results of light absorption by bpyH₂⁺, energy transfer to [NbO(C₂O₄)₃]³⁻, and electron transfer from the excited anion back to the cation producing blue cation-radical bpyH₂^{•+}. Coordinated oxalate ligands serve as a source for highly reducing anion-radical CO₂⁻ which propagates the formation of the blue paramagnetic centres (reduced bpy species) deeper in the bulk of the sample. The key role in the photoactivity is played by niobium coordinated oxalate, since (bpyH₂)C₂O₄ is not photoactive. These findings suggest a possibility of using niobium oxalates in photochemical processes, with potential applications in solar cells, photocatalysis, smart materials, sensors *etc.*

Experimental

General information

(NH₄)[NbO(C₂O₄)₂(H₂O)₂]·3H₂O, 2,2'-bipyridine (bpy), 1,10-phenanthroline (phen) and 2-aminopyridine (2-NH₂-py) were used as purchased (Sigma Aldrich) without any purification. IR spectra (4000–400 cm⁻¹) were recorded on a Scimitar FTS 2000 spectrometer. Elemental analysis was carried out on a Eurovector EA 3000 CHN analyser.

Synthesis of (bpyH₂)(bpyH)[NbO(C₂O₄)₃]·2H₂O (1)

0.04 g (0.26 mmol) of solid bpy was added to a clear solution of 0.1 g (0.26 mmol) of Nb-Ox in 4 mL of distilled water. The mixture was kept at 80 °C for 30 min until total dissolution of

bpy. Then the solution was cooled and the product was allowed to crystallise at 5 °C overnight. The crude product was collected by filtration, washed with ethanol and dried *in vacuo*. A typical yield was 0.130 g (71%). Anal. calcd for C₂₆H₂₂N₄NbO₁₅ C, H, N (%): 44.1, 3.3, 7.8. Found C, H, N (%): 43.8, 3.0, 7.9. IR (KBr, cm⁻¹): 3509 (m), 3377 (w), 3192 (w), 3099 (m), 2922 (m), 2849 (m), 2132 (w), 1716 (vs), 1682 (vs), 1649 (vs), 1594 (s), 1556 (m), 1518 (m), 1487 (s), 1436 (s), 1387 (vs), 1269 (s), 1233 (s), 1199 (s), 1096 (w), 1060 (w), 1000 (w), 898 (s), 803 (vs), 756 (m), 712 (w), 613 (m), 543 (m), 510 (m), 470 (m).

Synthesis of (phenH)₃[NbO(C₂O₄)₃]·3H₂O (2)

Aqueous solution (5 mL) of phen (0.1 g, 0.56 mmol) was added dropwise to an aqueous solution (5 mL) of Nb-Ox (0.218 g, 0.56 mmol) under stirring. Then the solution was kept at 80 °C for 30 min and after cooling to room temperature it was transferred to the fridge for crystallization at 5 °C overnight. The crude product was collected by filtration and dried *in vacuo*. A typical yield was 0.123 g (23%), the phase purity was checked by XRPD (Fig. S20†). Anal. calcd for C₄₂H₃₃N₆NbO₁₆ C, H, N (%): 52.0, 3.4, 8.7. Found C, H, N (%): 51.6, 3.0, 8.3. IR (KBr, cm⁻¹): 3583 (m), 3485 (m), 3072 (m), 2096 (w), 2002 (w), 1728 (s), 1706 (vs), 1670 (vs), 1615 (s), 1597 (s), 1542 (s), 1497 (m), 1472 (m), 1450 (m), 1378 (vs), 1320 (m), 1251 (s), 1190 (m), 1148 (m), 997 (w), 900 (s), 885 (m), 850 (s), 817 (m), 797 (s), 773 (s), 719 (s), 620 (m), 541 (m).

Synthesis of (2-NH₂-py)₃[NbO(C₂O₄)₃]·2H₂O (3)

Aqueous solution (5 mL) of 2-NH₂-py (0.1 g, 1.06 mmol) was added dropwise to the aqueous solution (5 mL) of Nb-Ox (0.417 g, 1.06 mmol) under stirring. Then the solution was kept at 80 °C for 30 min and after cooling to room temperature it was transferred to the fridge for crystallization at 5 °C overnight. The crude product was collected by filtration and dried *in vacuo*. A typical yield 0.133 g (18%). Anal. calcd for C₂₁H₂₅N₆NbO₁₅ C, H, N (%): 36.3, 3.7, 12.1. Found C, H, N (%): 37.0, 3.4, 12.3. IR (KBr, cm⁻¹): 3588 (w), 3399 (m), 3335 (m), 3215 (s), 3109 (s), 2968 (m), 2692 (w), 1707 (vs), 1686 (vs), 1648 (vs), 1601 (m), 1531 (s), 1395 (vs), 1255 (m), 1198 (m), 1110 (w), 997 (m), 900 (m), 835 (m), 798 (s), 565 (m), 516 (m), 474 (m), 419 (w).

Synthesis of (bpyH₂)(C₂O₄) (4)

0.1 g (0.64 mmol) of solid bpy was added to a clear solution of 0.08 g (0.64 mmol) of oxalic acid in 5 mL of distilled water. The mixture was kept at 80 °C for 30 min until total dissolution of bpy. Then the solution was cooled and the product was allowed to crystallise at 5 °C overnight. The crude product was collected by filtration and dried *in vacuo*. A typical yield was 0.130 g (78%). Anal. calcd for C₁₂H₁₀N₂O₄ C, H, N (%): 58.6, 4.1, 11.4. Found C, H, N (%): 59.0, 4.1, 11.4. IR (KBr, cm⁻¹): 3445 (w), 3102 (m), 3071 (m), 3058 (m), 3007 (w), 2925 (w), 2418 (m), 1995 (m), 1731 (s), 1607 (s), 1491 (m), 1405 (s), 1230 (s), 1205 (s), 1060 (s), 1009 (m), 815 (vs), 725 (s), 638 (s), 485 (m), 455 (m), 397 (w).

X-ray diffraction

Crystallographic data and refinement details for 1–3 are shown in Table S1 (see the ESI†). The diffraction data were collected using a New Xcalibur (Agilent Technologies) diffractometer with MoK α radiation ($\lambda = 0.71073$) by performing ω scans of narrow (0.5°) frames at 130 K. Absorption correction was done empirically using SCALE3 ABSPACK (CrysAlisPro, Agilent Technologies, Version 1.171.37.35 (release 13-08-2014 CrysAlis171 .NET) (compiled Aug 13 2014,18:06:01)). The structure was solved by direct methods and refined by full-matrix least-squares treatment against $|F|^2$ in anisotropic approximation with SHELX 2017/1⁵¹ in the ShelXle program.⁵² Hydrogen atoms for 1–3 were found directly and refined with -1.2 thermal ellipsoid parameters. Hydrogen bond parameters are summarised in Tables S3–S5.† The crystallographic data have been deposited in the Cambridge Crystallographic Data Centre under the deposition codes CCDC 1581634–1581636.

Photoactivity

UV absorption spectra in aqueous solutions were recorded using an Agilent 8453 spectrophotometer (Agilent Technologies). Diffuse reflection (DR) spectra for powder samples were recorded using a SF-56 spectrophotometer with the diffuse reflection accessory PDO-6 (LOMO, Russia). Kubelka–Munk function was used for the analysis of spectra. Stationary photolysis was performed using the radiation of a high-pressure mercury lamp with a set of glass filters for separating necessary wavelengths. In several experiments, an excimer XeBr lamp (excilamp) was used as a quasicontinuous source of UV-irradiation at 282 nm (half width of light pulse, 5 nm; pulse duration, 1 μ s; frequency, 200 kHz; incident light flux, 2.7×10^{16} photons $\text{cm}^{-2} \text{s}^{-1}$).⁵³ ESR spectra were recorded using an EMS spectrometer (Bruker). Free radicals were produced either by irradiation of a high pressure mercury lamp directed to the ESR cavity or by excilamp irradiation before placing the sample into the cavity.

Computational details

The molecular geometry of complex 1 was fully optimised using restricted and unrestricted density functional theory (DFT) in the gas phase, with different (odd) values of spin multiplicity. The initial guess of the atomic spatial coordinate was taken from the experimental structure. We compared the results obtained using different popular functionals. In particular, we chose hybrid (*viz.* B3LYP,⁵⁴ PBE0,⁵⁵ and M06-2X⁵⁶) and long-range corrected (*viz.* CAM-B3LYP⁵⁷ and ω B97X-D⁵⁸) functionals. The D3 version of Grimme's semi-empirical dispersion with Becke–Johnson damping GD3BJ⁵⁹ was also included for the B3LYP, PBE0, and CAM-B3LYP functionals. These functionals were coupled with the Pople 6-311++G** triple- ζ basis set for H, C, N, and O, the LANL2TZ(f) triple- ζ basis set on the Nb valence (the outer 13 electrons) and the LANL2TZ(f) effective core potential on the Nb core (the inner 28 electrons).^{60–62}

The vibrational frequencies and thermochemical values were subsequently computed at the same levels of theory, with

the harmonic approximation at $T = 298.15$ K and $p = 1$ atm, and no imaginary frequencies were found. The most stable state was found to be a singlet.

The UV-Vis absorption spectra for the equilibrium geometries of the ligand were calculated using time-dependent density functional theory (TD-DFT) accounting for $S_0 \rightarrow S_n$ ($n = 1$ to 50). The energy of the first 50 triplet states was also computed. The nature of the vertical excited electronic state was analysed. This investigation was performed by employing the long-range corrected functional ω B97X-D coupled with the same basis sets used for the optimization and frequency calculation, using the optimised geometry obtained with the M06-2X functional. The first bright singlet $S(\pi, \pi^*)$ excited state geometry was optimised using analytical gradients. This investigation was performed by employing the long-range corrected functional ω B97X-D coupled with the same aforementioned basis sets. The molecular geometry of the ground state was subsequently re-optimised starting from the optimised geometry of the first bright excited state using coupling of the M06-2X functional with the aforementioned basis sets. The optimization algorithm found another local minimum of the ground state potential energy hypersurface, rather close to the optimised geometry of the excited state. The vibrational frequencies and thermochemical values were subsequently computed at the same levels of theory, with the harmonic approximation at $T = 298.15$ K and $p = 1$ atm, and no imaginary frequencies were found. This second minimum geometry was subsequently used for computing the UV-Vis absorption spectrum at the TD-DFT level (functional ω B97X-D, same basis set combination), accounting for $S_0 \rightarrow S_n$ ($n = 1$ to 50), along with the energies of the first 50 triplet states. The nature of the vertical excited electronic state was analysed. In addition, in both absorption spectra, the vibronic progressions of the transition were simulated including Duschinsky and Herzberg–Teller effects.

The atomic charge population analysis, electric multiple moments, electronic density, and electrostatic potential were also computed within the Mulliken partition scheme for both the ground and singlet excited (vertical and relaxed) states.

To investigate the presence and nature of the possible intramolecular hydrogen bonding interactions, the non-covalent interaction (NCI) index combined with the second derivative of the reduced density gradient and the second main axis of variation was employed.^{63,64}

The singlet–singlet exciton coupling matrix element was computed through the transition density approach.^{65–67} To this aim, the system was partitioned in three moieties: two donors (represented by the bpyH ligands) and an acceptor (represented by the central core). The transition densities from the ground to the first bright excited state for the three moieties were computed at TD-DFT ω B97X-D coupled with the same aforementioned basis sets.

The molecular structure of radicals $[\text{NbO}(\text{C}_2\text{O}_4)_3]^{2+\cdot}$ and $(\text{bpyH})^{2+\cdot}$ was also fully optimised at the U-DFT level (doublets), using the M06-2X functional coupled with the same aforementioned basis sets. The total spin density (difference

between α and β densities) was also computed. The ESR g -tensor was also computed for $(\text{bpyH})^{2+}$, at the U-DFT level, using the B3LYP functional coupled with Barone's triple- ζ EPR-III basis set.⁶⁸

For the RDG analyses and exciton coupling calculations, the integration grid for the electronic density was set to 150 radial shells and 974 angular points. For the other calculations, the integration grid was set to 99 radial shells and 590 angular points. The convergence criteria for the self-consistent field were set to 10^{-12} for the RMS change in the density matrix and 10^{-10} for the maximum change in the density matrix. The convergence criteria for optimizations were set to 2×10^{-6} a.u. for the maximum force, 1×10^{-6} a.u. for the RMS force, 6×10^{-6} a.u. for the maximum displacement and 4×10^{-6} a.u. for the RMS displacement.

The calculation of the RDG and its derivatives and the calculation of the exciton coupling that were performed using homemade codes. The EPR g -tensor was computed using the ORCA 4.0.1 package.⁶⁹ All the other calculations were performed using the GAUSSIAN G09.D01 package.⁷⁰

Conflicts of interest

There are no conflicts to declare.

Acknowledgements

This work was supported by the Russian Science Foundation (grant number 14-13-00645). E. B. expresses his gratitude to the Rector of the Novosibirsk State University, Prof. M. P. Fedoruk, for his invitation to visit the Novosibirsk State University and acknowledges the Novosibirsk State University program "5-100".

The computational investigation of the work was carried out thanks to the equipment kindly provided by the Siberian Supercomputer Center ICMMG SB RAS and "Supercomputing Center of the Novosibirsk State University" (<http://nusc.nsu.ru>).

Notes and references

- C. N. R. Rao, S. Natarajan and R. Vaidhyanathan, *Angew. Chem., Int. Ed.*, 2004, **43**, 1466–1496.
- R. Clément, S. Decurtins, M. Gruselle and C. Train, in *Molecular Magnets Recent Highlights*, Springer Vienna, Vienna, 2003, pp. 1–19.
- Z. Wang, D. Xiao and J. Liu, *RSC Adv.*, 2014, **4**, 44654–44658.
- B. C. Faust and R. G. Zepp, *Environ. Sci. Technol.*, 1993, **27**, 2517–2521.
- Y. Zuo and J. Holgne, *Environmental science and technology*, American Chemical Society, 1992, vol. 26.
- J. Chen, H. Zhang, I. V. Tomov and P. M. Rentzepis, *Inorg. Chem.*, 2008, **47**, 2024–2032.
- Z. Wang, C. Chen, W. Ma and J. Zhao, *J. Phys. Chem. Lett.*, 2012, **3**, 2044–2051.
- C. Liu, F. Li, X. Li, G. Zhang and Y. Kuang, *J. Mol. Catal. A: Chem.*, 2006, **252**, 40–48.
- K. S. Min, A. L. Rhinegold and J. S. Miller, *Inorg. Chem.*, 2005, **44**, 8433–8441.
- G. L. Glen, J. V. Silverton and J. L. Hoard, *Inorg. Chem.*, 1963, **2**, 250–255.
- B. Kojić-Prodić, Ž. Ruzić-Toroš, M. Šljukić and IUCr, *Acta Crystallogr., Sect. B: Struct. Crystallogr. Cryst. Chem.*, 1978, **34**, 2001–2002.
- D. Tranqui, P. Boyer, J. Laugier and P. Vulliet, *Acta Crystallogr., Sect. B: Struct. Crystallogr. Cryst. Chem.*, 1977, **33**, 3126–3133.
- F. A. Cotton, M. P. Diebold and W. J. Roth, *Inorg. Chem.*, 1987, **26**, 2889–2893.
- B.-L. Ooi, T. Shihabara, G. Sakane and K.-F. Mok, *Inorg. Chim. Acta*, 1997, **266**, 103–107.
- M. R. Spirlet, J. Rebizant, B. Kanellakopulos, E. Dornberger and IUCr, *Acta Crystallogr., Sect. C: Cryst. Struct. Commun.*, 1987, **43**, 19–21.
- A. Chadha, N. C. Jayadevan and K. D. S. Mudher, *Thermochim. Acta*, 1987, **111**, 67–74.
- U. Baisch and D. Braga, *CrystEngComm*, 2009, **11**, 40–42.
- M. Jurić, B. Perić, N. Brničević, P. Planinić, D. Pajić, K. Zadro, G. Giester and B. Kaitner, *Dalton Trans.*, 2008, 742–754.
- M. Šestan, B. Perić, G. Giester, P. Planinić and N. Brničević, *Struct. Chem.*, 2005, **16**, 409–414.
- G. Mathern and R. Weiss, *Acta Crystallogr., Sect. B: Struct. Crystallogr. Cryst. Chem.*, 1971, **27**, 1610–1618.
- N. Galešić, N. Brničević, B. Matković, M. Herceg, B. Zelenko, M. Šljukić, B. Prelesnik and R. Herak, *J. Less-Common Met.*, 1977, **51**, 259–270.
- L. Androš, M. Jurić, J. Popović, A. Šantić, P. Lazić, M. Benčina, M. Valant, N. Brničević and P. Planinić, *Inorg. Chem.*, 2013, **52**, 14299–14308.
- M. Jurić, P. Planinić, N. Brničević and D. Matković-Čalogović, *J. Mol. Struct.*, 2008, **888**, 266–276.
- L. A. Dubraja, D. Matković-Čalogović and P. Planinić, *CrystEngComm*, 2015, **17**, 2021–2029.
- Y. Zhang, L. Pei, Z. Zheng, Y. Yuan, T. Xie, J. Yang, S. Chen, J. Wang, E. R. Waclawik and H. Zhu, *J. Mater. Chem. A*, 2015, **3**, 18045–18052.
- A. G. S. Prado, L. B. Bolzon, C. P. Pedroso, A. O. Moura and L. L. Costa, *Appl. Catal., B*, 2008, **82**, 219–224.
- X. Fang, L. Hu, K. Huo, B. Gao, L. Zhao, M. Liao, P. K. Chu, Y. Bando and D. Golberg, *Adv. Funct. Mater.*, 2011, **21**, 3907–3915.
- H. Liu, N. Gao, M. Liao and X. Fang, *Sci. Rep.*, 2015, **5**, 7716.
- J.-M. Jehng and I. E. Wachs, *J. Raman Spectrosc.*, 1991, **22**, 83–89.
- A. Moissette, Y. Batonneau and C. Brémard, *J. Am. Chem. Soc.*, 2001, **123**, 12325–12334.
- B. D. Coleman and R. M. Fuoss, *J. Am. Chem. Soc.*, 1955, **77**, 5472–5476.

- 32 O. Poizat, G. Buntinx, P. Valat, V. Wintgens and M. Bridoux, *J. Phys. Chem.*, 1993, **97**, 5905–5910.
- 33 O. Poizat and G. Buntinx, *J. Phys. Chem.*, 1995, **99**, 9403–9407.
- 34 S. S. Ali, K. Maeda, H. Murai and T. Azumi, *Res. Chem. Intermed.*, 2003, **29**, 1–10.
- 35 V. Nadtochenko and J. Kiwi, *J. Photochem. Photobiol. A*, 1996, **99**, 145–153.
- 36 J. Chen, H. Zhang, I. V. Tomov, M. Wolfsberg, X. Ding and P. M. Rentzepis, *J. Phys. Chem. A*, 2007, **111**, 9326–9335.
- 37 I. P. Pozdnyakov, O. V. Kel, V. F. Plyusnin, V. P. Grivin and N. M. Bazhin, *J. Phys. Chem. A*, 2008, **112**, 8316–8322.
- 38 H. Dürr and H. Bouas-Laurent, *Photochromism: molecules and systems*, Elsevier, 2003.
- 39 C. S. Johnston, R. E. Visco, H. S. Gutowsky and A. M. Hartley, *J. Chem. Phys.*, 1962, **37**, 1580–1582.
- 40 A. Alberti, in *Organic Photochromic and Thermochromic Compounds*, Kluwer Academic Publishers, Boston, 1999, pp. 211–239.
- 41 O. Poizat, C. Giannotti and C. Sourisseau, *J. Chem. Soc., Perkin Trans. 2*, 1987, 829.
- 42 P.-X. Li, M.-S. Wang and G.-C. Guo, *Cryst. Growth Des.*, 2016, **16**, 3709–3715.
- 43 G. M. Hassan, U. Ulusoy and M. Ikeya, *Jpn. J. Appl. Phys.*, 2000, **39**, 6236–6242.
- 44 F. J. Callens, R. M. H. Verbeeck, P. F. A. Matthys, L. C. Martens and E. R. Boesman, *Calcif. Tissue Int.*, 1987, **41**, 124–129.
- 45 A. S. Jeevarajan, I. Carmichael and R. W. Fessenden, *J. Phys. Chem.*, 1990, **94**, 1372–1376.
- 46 Y. Ilan and J. Rabani, *Int. J. Radiat. Phys. Chem.*, 1976, **8**, 609–611.
- 47 G. Williams and D. C. Watts, *Trans. Faraday Soc.*, 1970, **66**, 80–85.
- 48 V. A. Tolkmachev, *J. Mol. Liq.*, 2000, **86**, 37–44.
- 49 V. F. Plyusnin, E. M. Glebov, V. P. Grivin, V. V. Korolev, A. V. Metelitsa, N. A. Voloshin and V. I. Minkin, *Russ. Chem. Bull.*, 2011, **60**, 124–131.
- 50 E. Benassi, B. Carlotti, C. G. Fortuna, V. Barone, F. Elisei and A. Spalletti, *J. Phys. Chem. A*, 2015, **119**, 323–333.
- 51 G. M. Sheldrick, *Acta Crystallogr., Sect. A: Found. Adv.*, 2015, **71**, 3–8.
- 52 C. B. Hübschle, G. M. Sheldrick and B. Dittrich, *J. Appl. Crystallogr.*, 2011, **44**, 1281–1284.
- 53 E. A. Sosnin, T. Oppenländer and V. F. Tarasenko, *J. Photochem. Photobiol. C*, 2006, **7**, 145–163.
- 54 A. D. Becke, *J. Chem. Phys.*, 1993, **98**, 5648–5652.
- 55 C. Adamo and V. Barone, *J. Chem. Phys.*, 1999, **110**, 6158–6169.
- 56 Y. Zhao and D. G. Truhlar, *Theor. Chem. Acc.*, 2008, **120**, 215–241.
- 57 T. Yanaia, D. P. Tew and N. C. Handy, *Chem. Phys. Lett.*, 2004, **393**, 51–57.
- 58 J.-D. Chai and M. Head-Gordon, *J. Chem. Phys.*, 2008, **128**, 84106.
- 59 S. Grimme, S. Ehrlich and L. Goerigk, *J. Comput. Chem.*, 2011, **32**, 1456–1465.
- 60 P. J. Hay and W. R. Wadt, *J. Chem. Phys.*, 1985, **82**, 299–310.
- 61 W. R. Wadt and P. J. Hay, *J. Chem. Phys.*, 1985, **82**, 284–298.
- 62 P. J. Hay and W. R. Wadt, *J. Chem. Phys.*, 1985, **82**, 270–283.
- 63 H. J. Bohórquez, C. F. Matta and R. J. Boyd, *Int. J. Quantum Chem.*, 2010, **110**, 2418–2425.
- 64 E. R. Johnson, S. Keinan, P. Mori-Sánchez, J. Contreras-García, A. J. Cohen and W. Yang, *J. Am. Chem. Soc.*, 2010, **132**, 6498–6506.
- 65 G. D. Scholes and D. L. Andrews, *J. Chem. Phys.*, 1998, **107**, 5374–5384.
- 66 B. P. Krueger, G. D. Scholes and G. R. Fleming, *J. Phys. Chem. B*, 1998, **102**, 5378–5386.
- 67 E. Benassi and S. Corni, *J. Phys. Chem. C*, 2013, **117**, 25026–25041.
- 68 G. De Luca, T. Mineva, N. Russo, E. Sicilia and M. Toscano, Continuum dielectric models for the solvent and density functional theory: the state-of-the-art, in *Recent advances in density functional methods. Part II*, ed. D. Chong, World Pub., Singapore, 1997, pp. 41–59.
- 69 F. Neese, *Comput. Mol. Sci.*, 2012, **2**, 73–78.
- 70 M. J. Frisch, G. W. Trucks, H. B. Schlegel, G. E. Scuseria, M. A. Robb, J. R. Cheeseman, G. Scalmani, V. Barone, G. A. Petersson, H. Nakatsuji, X. Li, M. Caricato, A. Marenich, J. Bloino, B. G. Janesko, R. Gomperts, B. Mennucci, H. P. Hratchian, J. V. Ortiz, A. F. Izmaylov, J. L. Sonnenberg, D. Williams-Young, F. Ding, F. Lipparini, F. Egidi, J. Goings, B. Peng, A. Petrone, T. Henderson, D. Ranasinghe, V. G. Zakrzewski, J. Gao, N. Rega, G. Zheng, W. Liang, M. Hada, M. Ehara, K. Toyota, R. Fukuda, J. Hasegawa, M. Ishida, T. Nakajima, Y. Honda, O. Kitao, H. Nakai, T. Vreven, K. Throssell, J. A. Montgomery, J. E. Peralta, F. Ogliaro, M. Bearpark, J. J. Heyd, E. Brothers, K. N. Kudin, V. N. Staroverov, T. Keith, R. Kobayashi, J. Normand, K. Raghavachari, A. Rendell, J. C. Burant, S. S. Iyengar, J. Tomasi, M. Cossi, J. M. Millam, M. Klene, C. Adamo, R. Cammi, J. W. Ochterski, R. L. Martin, K. Morokuma, O. Farkas, J. B. Foresman and D. J. Fox, *Gaussian 09*, 2008.